Refinement of Falsified Depth Maps for the SwissRanger Time-of-Flight 3D Camera on Autonomous Robots

Isaac O. Osunmakinde, *MIEEE*

Mobile Intelligent Autonomous Systems, Modelling and Digital Sciences Department,
Council for Scientific and Industrial Research (CSIR),
P O Box 395 Pretoria 0001, South Africa
iosunmakinde@csir.co.za

Abstract—**Robot navigation depends on accurate scene analysis by a camera using its data. This paper investigates a refinement of the inherent falsified depth maps generated from a 3D SwissRanger camera in the emission of beams of rays through a modulated infrared light channel affected by environmental noise. The SR4000 time-of-flight camera produces streams of depth maps projected as a 2.5D on an x-y plane, which are refined using a dynamic convolution filter method coupled with a hypergraph-type model. Our findings indicate that the range of the camera is experimentally confirmed as being nine metres; more extreme values of impulse noise pixels are detected outside the range; while the uniform noise of valid pixel values affects depth maps of objects formed within the range. A decrease in the window size of filtering, to a pixel level, minimizes both the falsified depth maps of corrupted frames and the dominant effect of the noise pixels, to an acceptable level. The performance of our approach in the absence of complementing time-of-flight (ToF) with other camera types exhibits reliable depth maps for promising field work in terms of visual quality, mean squared error (MSE), root mean squared error (RMSE), and peak signal-to-noise ratio (PSNR).**

Keywords-component; Computer Vision, SwissRanger Camera; Image Pixel; Depth Map; Noise; Refinement; Robot

I. INTRODUCTION

Safety and security in autonomous navigation constitute some of the significant objectives of robotic technology [1]. Researchers and practitioners have stressed that autonomous robot navigation along rough terrains, such as outdoor environments, is an ongoing key challenge [1] [2]. In practice, one could say that rough terrains may be defined as possessing different percentages of mingled features within the different parts (left side, right side and centre) of a scene frame, perceived by a robot sensor as a beam of depth scan. To complicate the challenge further, robots are now deployed for underground mining where 3D data sensing is required. This application demands estimation of accurate depths of objects and building realistic maps of such rough and dangerous mining environments. Existing and alternative 3D sensors, such as structured light cameras and laser range finders, are complex, expensive, and often require expert knowledge to operate [3] [4].

3D data perception is becoming increasingly essential in the scanning market and in application scenarios, such as robotics in mining. The SwissRanger SR4000 ToF 3D camera shown in Fig. 1(a) is mounted on a robot for sensing 3D images in this domain of interest. It offers a variety of benefits, such as measuring 3D depth maps at video rates with a resolution of 176x144 pixels, and it is an active sensor that measures the travel time of infrared light [5]. However, similar to other sensors using modulated light, the ToF camera suffers from ray-scattering due to inability to distinguish depths that are a multiple of wavelength of the modulated signal. Its image frames are susceptible to additional noise, which produces falsified depth maps. For instance, if an object (object A) obstructs the view of another (object B) within the camera's 9-metre range, the depth map of object B is distorted with unequal probabilities (see the 3 chairs adjacent to one another in Fig. 1(b)).

(a) ToF camera (b) Corrupted frame

Figure 1: Problem establishment of (a) a ToF camera; and (b) a corrupted frame with falsified depth maps.

The falsified depth map (noise) perceived on the corrupted frame appears to discourage the use of ToF cameras on autonomous robots. The noisy nature of the ToF camera in the above scenario affects the building of realistic maps, and may hinder the ability of robots to estimate the positions of obstacles accurately. This is problematic, as robots are increasingly being used in industry to improve safety and to save lives. The two major types of impulse noise, which arise

in digital image transmission over noisy channels or faulty sensors, are presented in literature as: (i) salt-and-pepper noise and (ii) uniform noise [6] [7]. In the former, corrupted pixels have extreme values and are easy to detect as they differ noticeably from their neighbours. In the latter, noisy pixels have valid values, which are more difficult to spot within the uncorrupted pixels. We observed that the salt-and-pepper noise appeared to be generated predominantly at a far-field outside the nine metre ToF range, while the uniform noise appears to be generated more within the camera's range, similar to the example in Fig. 1. Since the noise outside the ToF range can be ignored in the camera and the depth of an obstacle is important to a robot's navigation, our experimental knowledge indicates that improving the depth map estimation within the camera's range is manifestly a sound basis for optimising the ToF perception.

Several references in [8] [9] [10] [11] have presented some sophisticated noise correction methods, including camera calibration, fusion, and related noise removal methods. In [8], a distance calibration approach for Photonic Mixer Device (PMD)-based sensing is presented. The process includes a lateral and distance calibration technique where the camera's intrinsic parameters are estimated. In [9], a PMD-stereo fusion algorithm is used to combine patchlets from the PMD-stereo camera. Least-square method is used to estimate 3D patchlets from PMD range images as well as from a pair of stereo images. Jiejie Zhu et al. [10] mention that fusion of the ToF depth and stereo can be used for obtaining accurate depth maps. They introduce a method for combining the results from both image capturing methods, to render a result that performs better than either method alone. A depth probability distribution function from each method is calculated and then merged. In contrast, the ToF devices are typically poorly calibrated [10].

Related to this work is also research on restoration from noise introduced in the intensity of 2D images using filtering methods [11]. Classical mean filter is said to remove the noise, but it leaves out a few isolated stars in image as a result of its inability to distinguish between original and noisy pixels. Hence, unrepresentative pixel values participate in the filtering process, which degrades the image. Consequently, the application of the filtering approaches to refine ToF noise is hardly mentioned, perhaps due to this limitation. The motivation of the experiment presented in this paper is to emphasise that reliable depth maps, using ToF cameras in the absence of other types of cameras, are feasible. This is investigated with a dynamic convolution filter based on a hypergraph model, which improves the limitation of using the classical mean filter alone. The major contributions in this paper are as follows:

- The application of the dynamic convolution filter based on a hypergraph model, to the ToF noise, which improves a limitation of distinguishing pixels in classical mean filters.
- The refinement of falsified depth maps is evaluated on a real-life ToF data stream using only ToF cameras in the absence of other camera types.

The rest of the paper is arranged as follows: section II presents the theoretical background, which includes operation of the ToF cameras and modelling of noise pixels; section III presents the depth map refinement which includes the convolution filter, hypergraph and pixel neighbourhood, and our refinement approach; section IV critically presents visual inspection and quantitative experimental evaluations of the approach using lightly and heavily corrupted ToF images, and five noise levels. Our refinement approach is also benchmarked with a popular Lena image. We conclude the paper in section V.

II. THEORETICAL BACKGROUND

A. Operation of the ToF Camera

The SwissRanger SR4000 time-of-flight camera [5] is used for acquiring 3D range data with a resolution of 176x144 pixels. The camera emits infrared light which illuminates a scene and allows the depth of each pixel to be measured based on the arrival time of the modulated light. Unlike a laser scanner, which repeatedly scans scene points for a depth map, the ToF advantageously scans full frame depth at once. However, being a camera that uses phase differences of modulated light, it suffers from challenging noise associated with rapid movement. More information about the ToF camera can be found in [12].

B. Modelling of Noise Pixels

Since errors or false depths are introduced in the noisy communication channel or imaging sensor, such as the ToF camera, there are two main models for describing most noise in digital images. These models are [13]: (i) additive Gaussian and (ii) impulse noise models. The additive Gaussian noise model is formulated as equation (1).

$$x_{ij}^n = x_{ij}^o + n_{ij} \tag{1}$$

x_{ij}^n indicates the noisy pixel (i, j), x_{ij}^o indicates the original pixel and n_{ij} is the added noise. This type of model describes the salt-and-pepper noise. The impulse noise replaces a pixel value with a random value and is formulated as equation (2).

$$x_{ij}^n = \begin{cases} n_{ij} & p \\ x_{ij}^o & (1-p) \end{cases} \tag{2}$$

p is a probability which is equal to noise rate in the image. This type of model describes the uniform noise. Since both noise types are perceived on the same ToF image frame, the variation pattern is less dependent on the type of noise. A combined approach is required to mitigate the dominant effects of the noise.

A.   Convolution Filter

The convolution filter considered herein is the mean filter [14] [18], which is characterised as a low-pass box filtering. It smoothes images as it is often used to minimise noisy pixels. In its process, it convolves a kernel with a noisy image where it replaces each pixel value with the mean value of its neighbours, including the target pixel. The process is adopted from a Sobel operator [15] and is described as shown in equation (3) for a noisy image $I(x, y)$ with a filter kernel $W(k, k)$.

$$I'(x, y) = I(x, y) \otimes W(k, k) \qquad (3)$$

$I'(x, y)$ is a filtered image and $\otimes$ is a convolution operator. The size of the neighbourhood or kernel used is paramount to the performance of the filter [16]. The most commonly-used kernel sizes are 3x3, 5x5, 7x7, etc. The filter is characterised by the fact that an increase in the kernel size increases the smoothing performance, but the image gets blurred. This implies that the choice of the convolution kernel size is a trade-off between noise reduction and blurring effect. The trade-off can be balanced or optimised using the concept of a hypergraph model, as explained in subsection B.

B.   Hypergraph and Pixel Neighbourhood

A hypergraph H [14] is a pair (X, ξ) consisting of a non-empty finite set X and a family $\xi = (E_i)_{i \in I}$ of non-empty subsets of X called hyperedges, with equation (4).

$$\bigcup_{i \in I} E_i = X, I = \{1,2,3,...,n\}, \qquad n \in N \qquad (4)$$

Considering star of H with centre at x: For $x \in S$, a star of H (with centre x) is the set of hyperedges of H which contain x and is denoted by $H(x)$. The degree of x is the cardinality of the star $H(x)$ denoted $d(x) = card(H(x))$. Otherwise, the neighbourhood of vertex $x \in X$ is the set Γ_x formed by all vertices adjacent to x. In image analysis, a hypergraph associates a pixel x to its neighbourhood and forms a star with $d(x) = 3$, 4, or 8 neighbours of a point. Since the choice of $d(x)$ often depends on the image application, this work primarily uses the maximum of $d(x)$, which conditionally reduces in size subject to alleviating the limitation of classical mean filter.

Similar to other convolution filters, classical mean filter is known to have the limitation of not distinguishing original pixels from noise pixel values, which can significantly affect the mean value of the neighbouring pixels. This issue is mitigated with a dynamic convolution kernel in our approach in subsection C.

C.   The Refinement Approach

This refinement approach begins with the construction of a pixel's neighbourhood. These hypergraph neighbourhoods vary dynamically in kernel size. In order to balance between noise reduction and blurring effect in the choice of kernel size, a hypergraph of eight-neighbours of a point, as in Fig. 2(a), is used. This controls the excessive usage of a pixel's neighbourhood. It also ensures direct influences to a centre pixel in relation to the 3x3 kernel shown in Fig. 2(b). The primary 3x3 size of the kernel changes dynamically as it is conditioned on the presence of noise pixels in the neighbourhood of a pixel. Before every convolution filtering, detected noise pixels are eliminated from the process since they can ripple errors through the mean value computed from the pixel's neighbourhood. This addresses a limitation with the classical mean filtering using the noise detector scheme in [16].
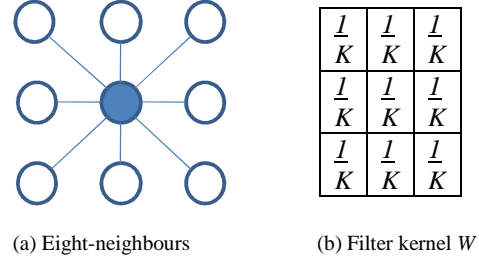

(a) Eight-neighbours   (b) Filter kernel W

Figure 2: Transformation of (a) eight-neighbours of a centre pixel x [14], and (b) the primary filter kernel adopted from [15]

The scheme states that: (i) if a pixel x has at least one pixel y amongst the other eight pixels in the neighbourhood then pixel x is considered an original pixel and pixel y is deemed similar to pixel x; and (ii) if x does not have at least one similar pixel amongst its neighbours, it is considered a noisy and strange pixel as shown in equation (5).

$$x = \begin{cases} x_{ij}^o & K\{| x - y | \leq D_1\} \geq N_1^{th} \\ x_{ij}^n & else \end{cases} \qquad (5)$$

D_1 is adopted as the maximum depth difference between the similar x and y pixels and is often assumed to be eight as for Fig. 2(a). N_1^{th} is 1 as every pixel is assumed to be similar to at least 1 pixel, and K is the number of y pixels that satisfy equation (5) while the noisy pixels are eliminated. This implies that the value of the kernel size is modified as K changes, resulting in the use of the dynamic convolution kernel.

Otherwise, the convolution process in equation (3) is expatiated and described in equation (6), given that there is an image (I) of size M x N with a filter kernel (W) of size k x k subject to changes in k size. A sample computation of an output value for pixel I'_{22} is shown in equation (7). During process of the refining the boundary pixel values, the kernel values are padded with zeros. A clearer idea of the process adopted here can be obtained from the edge detection of Sobel operator in [15].

$$\begin{pmatrix} I_{11}^{'} & \cdots & I_{1n}^{'} \\ \vdots & \cdots & \vdots \\ I_{m1}^{'} & \cdots & I_{mn}^{'} \end{pmatrix} =$$

$$\begin{pmatrix} I_{11} & \cdots & I_{1n} \\ \vdots & \cdots & \vdots \\ I_{m1} & \cdots & I_{mn} \end{pmatrix} \otimes \begin{pmatrix} w_{11} & \cdots & w_{1k} \\ \vdots & \cdots & \vdots \\ w_{k1} & \cdots & w_{kk} \end{pmatrix} \quad (6)$$

$$I'_{22} = (I_{11} * w_{11}) + (I_{12} * w_{12}) + (I_{13} * w_{13}) + \\ (I_{21} * w_{21}) + (I_{22} * w_{22}) + (I_{23} * w_{23}) + \\ (I_{31} * w_{31}) + (I_{32} * w_{32}) + (I_{33} * w_{33}) \quad (7)$$

D. Scoring and Evaluation Scheme

In this section, the performance of our proposed approach is studied through visual inspection as well as quantitatively. During visual inspection, one compares the quality of the pixel values of corrupted frames with those of refined image frames. The following evaluation models were chosen as quantitative refinement scoring schemes [17]: (i) the mean squared error (MSE), (ii) the root mean squared error (RMSE), and (iii) the peak signal-to-noise ratio (PSNR). The schemes are described in equations (8), (9), and (10) respectively.

$$MSE = \frac{1}{MN} \sum_{i=1}^{MN} (y_i - \hat{y}_i)^2 \quad (8)$$

$$RMSE = \sqrt{\frac{1}{MN} \sum_{i=1}^{MN} (y_i - \hat{y}_i)^2} \quad (9)$$

$$PSNR = 10 \log_{10} \frac{255^2}{MSE} \quad (10)$$

y_i and $\hat{y}_i$ denote the pixel values of the refined and the original image respectively, and $M \times N$ is the ToF image size. In this work, y_i and $\hat{y}_i$ are also used to denote the pixel values of the corrupted and of the original images. They are used as objective evaluation schemes for the refined frames. Lower scoring results for both MSE and RMSE, and higher scoring results for PSNR based on the rate of noise are expected and preferred.

IV. EXPERIMENTAL EVALUATIONS

One of the objectives of this paper is to apply the theory of our proposed approach in practice by emphasising applications and carrying out practical work on refining the corrupted depth maps. The ToF captures daylight scenes and produces a stream of noisy image frames projected as a 2.5D on an x-y plane. An original noisy frame is shown in Fig. 3(a). An obstructing body is set to move towards the SR4000 3D ToF camera from a distance, generating increased noise. Again, the

range of the camera is experimentally confirmed as nine metres and, the size of an image frame is 176x144 pixels. Extreme values of the impulse noise pixels appear to be generated more outside the range, while uniform noise of valid pixel values is observed affecting the depth maps of objects formed within the range.

Since the correct depths of obstacles are important to the robot's navigation, the emphasis is on the depths of the three chairs placed adjacent to one another within the ToF range as shown in Fig. 3(a). The performance of the noise refinement approach is compared on lightly and heavily corrupted frames. A heavily corrupted frame is when the obstructing body appears closest to the ToF's light emission and is estimated to have generated a 90% noise level, as shown in Fig. 4(b). A lightly corrupted frame, on the other hand, has a noise level of 10%, as shown in Fig. 3(b). This work focuses more on the refinement of the noise introduced and generated by the moving body within the range. This type of noise is more difficult to spot within the uncorrupted pixel values. In terms of performance measures, the MSE, RMSE, and PSNR are computed when evaluating the original depth frames against the refined and the corrupted frames as shown in Table 1.

A. Observations for Lightly Corrupted ToF Images

The objective here is to access the qualitative performance of our refinement approach on lightly corrupted ToF images which exhibit noticeable differences when compared to the heavily corrupted images in Fig. 4(b). In particular, Fig. 3(b) contains a 10% noise level as it captures the state of the obstructing moving body being a distance from the ToF.
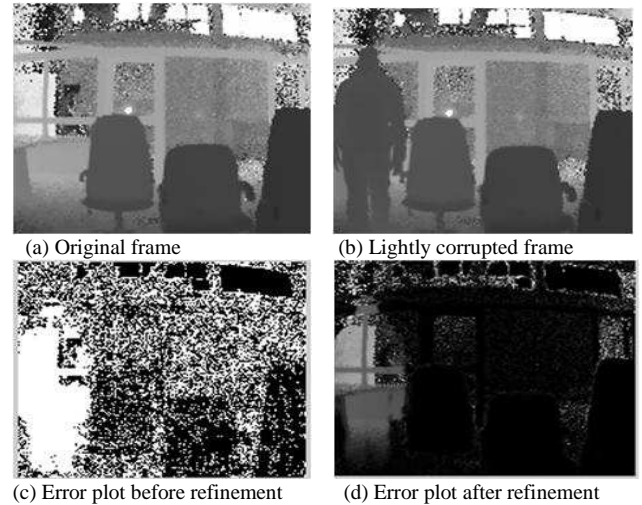

(a) Original frame (b) Lightly corrupted frame

(c) Error plot before refinement (d) Error plot after refinement

Figure 3: A 2.5D depth map frame from an indoor data stream: (a) original noisy frame from the ToF; (b) corrupted frame due to a moving body; (c) error plot before refinement; and (d) error plot after refinement equivalent to the expected result.

Fig. 3(b) indicates that the noise introduced is light, which may not be noticeable when compared to Fig. 3(a). Fig. 3(c) indicates the error plot reconstructed before refinement. Fig. 3(d), on the other hand, is the error plot reconstructed after refinement, based on our approach. Although, in an ideal camera situation, the background of Fig. 3(c) would be dark

and the foreground (moving body) lighter in colour, one can observe that the falsified depths are minimised to an acceptable level in Fig. 3(d).

B. Observations for Heavily Corrupted Images

Again, the objective here is to access the qualitative performance of our approach on heavily corrupted ToF images which are noticeably different from the lightly corrupted ones in Fig. 3(b). In particular, Fig. 4(b) contains a 90% noise level as it captures the state of the obstructing body being right in front of the ToF. In Fig. 4(b), it can be seen that the noise introduced is heavy and very noticeable, compared to that in Fig. 4(a). This results in more white clusters on the error plot reconstructed before refinement in Fig. 4(c). On the other hand, Fig. 4(d) is the error plot reconstructed after refinement, according to our approach. It can also be observed that the falsified depths are minimised to an acceptable level in Fig. 4(d).
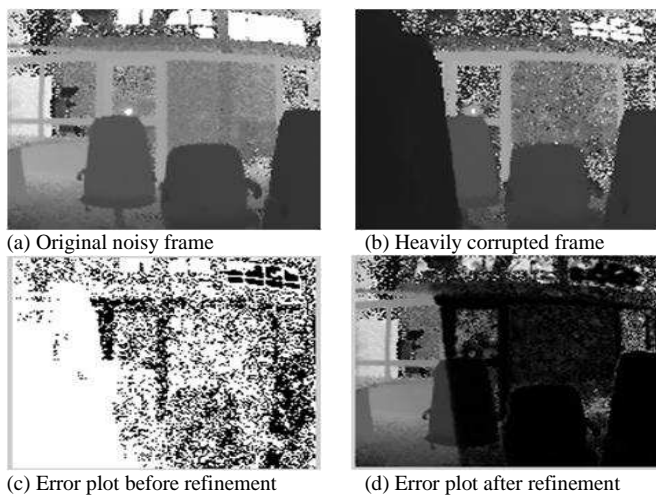

(a) Original noisy frame

(b) Heavily corrupted frame

(c) Error plot before refinement

(d) Error plot after refinement

Figure 4: A 2.5D depth map frame from an indoor data stream: (a) original noisy frame from the ToF; (b) corrupted frame due to a moving body; (c) error plot before refinement; and (d) error plot after refinement tends towards the expected result.

C. Performance on the ToF Image Refinement

From the results in Table 1, we specifically access the quantitative performance of our approach with respect to noise levels ranging between 10% and 90%.

Table 1: Comparing the refined and corrupted images based on the noise levels.

Noise Level (%)	Refined			Corrupted		
	RMSE	MSE	PSNR	RMSE	MSE	PSNR
10	45.98	8.29	63.01	49.93	9.77	62.29
30	53.22	11.19	61.74	56.20	12.39	61.26
50	63.72	15.91	60.18	66.02	17.09	59.86
70	81.80	26.24	58.01	85.40	28.61	57.63
90	122.6	23.31	58.52	126.20	25.88	58.06

Having compared the original and corrupted frames, as well as the original and refined frames, the results of the MSE, the RMSE, and the PSNR are shown in Figs. 5, 6, and 7 respectively. In Figs. 5 and 6 one can see that the trend of the refinement results minimise the noise significantly compared to the trend showing the corrupted pixels. This justifies the fact that lower scoring results are better for the MSE and the RMSE. On the other hand, the PSNR measures the refinement performance with higher scores over the corrupted frames. The higher scores confirm a constructive refinement of our approach relating to the corrupted frames.
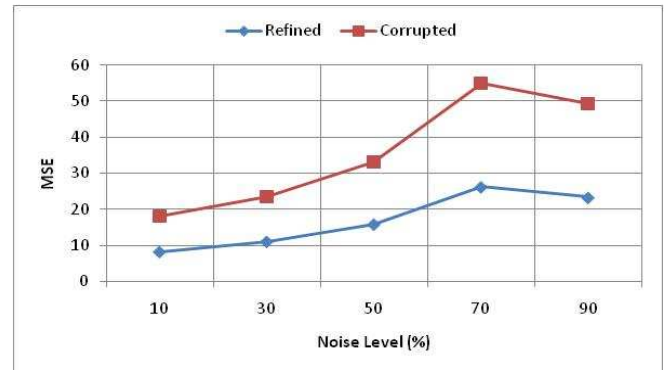

Figure 5. The MSE at various noise levels for the refined image is lower than that of the corrupted image when compared to the original frames.
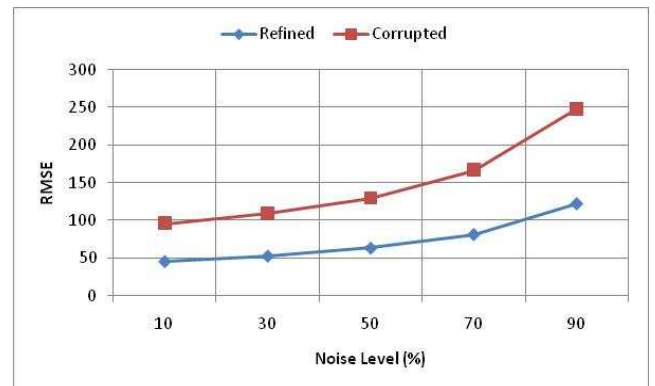

Figure 6. The RMSE at various noise levels for refined image is lower than that of the corrupted image when compared to the original frames.
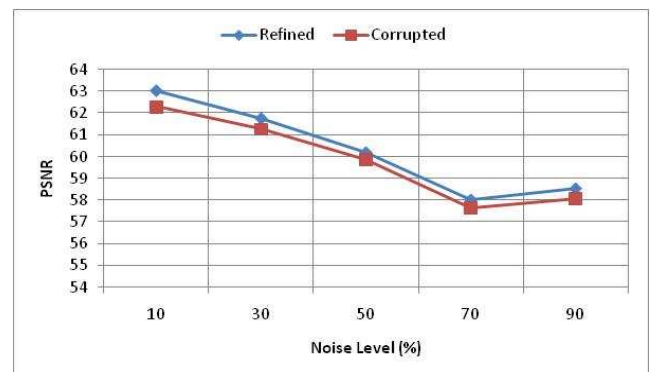

Figure 7. The PSNR at various noise levels for the refined image is higher (or greater) than that of the corrupted image when compared to the original frames.

It can be seen that the quantitative results here correspond to each other and match the noise reduction results in the visual quality of subsections A and B.

D. Validating Performance with Popular 2D Lena Image

To validate our refinement performance using the visual quality, a popular 2D Lena image from [11] is used as a benchmark. The noisy Lena image in Fig. 8(b) is provided for refinement and the result in Fig. 8(c) is obtained using our approach which is almost equivalent to the noise free image in Fig. 8(a). The objective of this paper is focused on refining the falsified depth maps on ToF images.

(a) Noise free image   (b) Noisy image   (c) Refined image

Figure 8: Validating our refinement approach with the popular 2D Lena image [11], (a) Noise free image, (b) Noisy image, and (c) our refined image result.

E. Concluding Remarks

We have proposed and demonstrated the use of a dynamic convolution filtering based on a hypergraph model for the refinement of ToF noise pixels in the absence of complementing the ToF with other camera types. At first, the falsified depth map in Fig. 1 seems discouraging, but the experimental results on lightly and heavily corrupted frames in section 4 show that falsified depth maps from the ToF camera could be restored.

Our findings indicate that the range of the camera is experimentally obtained as being nine metres. More extreme values of impulse noise pixels are detected outside the range while uniform noise of valid pixel values affects the depth maps of objects formed within the ToF range. A decrease in the window size of filtering to a pixel level minimises both the falsified depths of corrupted data frames and the dominant effect of the noise pixels, to an acceptable level. In an ideal ToF situation, the expected result would be to have the background of the visual error maps dark and the foreground (moving body) lighter in colour. One can see that most of the errors introduced by the moving body in Figs. 3(b) and 4(b), are refined when the reconstructed error plot results in Figs. 3(d) and 4(d) are compared with the error plot before refinement in Figs. 3(c) and 4(c). The original errors of the ToF in Figs. 3(a) and 4(a) are yet to be addressed properly as they seem to appear as white clusters outside the ToF range in Figs. 3(d) and 4(d). However, our approach exhibits reliable depth maps for promising field work in terms of good quantitative performance results, which includes mean squared error (MSE), root mean squared error (RMSE), and peak signal-to-noise ratio (PSNR) in Figs. 5, 6, and 7 respectively.

This research has been experimented on a stream of ToF data captured in daylight. In future work, the research can be explored further in different forms, including the following: (i) conduct experiments on a stream of ToF night frames; (ii) compare this method with other noise removal methods; (iii) improve refinement on the original ToF errors; (iv) carry out a field test on robots.

REFERENCES

[1] J. Minguez and L. Montano, "Sensor-based robot motion generation in unknown, dynamic and troublesome scenarios," Journal of Robotics and Autonomous Systems, vol. 52, pp. 290-311, 2005.

[2] M. J. Procopio, J. Mulligan, and G. Grudic, "Learning in dynamic environments with ensemble selection for autonomous outdoor robot navigation," In proceedings of the IEEE/RSJ International Conference on Intelligent Robots and Systems, ISBN: 978-1-4244-2057-5, 2008, pp. 620-627.

[3] S. Meers and K. Ward, "Head-Pose Tracking with a Time-of-Flight Camera," in proceedings of the Australian Conference on Robotics and Automation, Canberra, Australia, 2008.

[4] Y. Cui, S. Schuon, D. Chan, S. Thrun, and C. Theobalt, "3D shape scanning with a time-of-flight camera," Computer Vision and Pattern Recognition (CVPR), 2010 IEEE Conference, ISBN: 978-1-4244-6984-0, pp. 1173-1180.

[5] A. Kolb, E. Barth, R. Koch, and R. Larsen, "Time-of-flight sensors in computer graphics," In Eurographics, State of the Art Reports, 2009, pp. 119-134.

[6] N. Alajlan, M. Kamel, and E. Jernigan, "Detail preserving impulsive noise removal," Signal Processing: Image Communication, vol. 19 (10), pp. 993–1003, 2004.

[7] W. Luo, "An efficient detail-preserving approach for removing impulse noise in images," IEEE Signal Processing Letters, vol. 13 (7), pp. 413–416, 2006.

[8] M. Lindner and A. Kolb, "Lateral and depth calibration of PMD-distance sensors," Advances in Visual Computing, pp. 524–533, 2006.

[9] C. Beder, B. Bartczak, and R. Koch. "A combined approach for estimating patchlets from pmd depth images and stereo intensity images," In Proc. DAGM, pp. 11–20, 2007.

[10] J. Zhu, L. Wang, R. Yang, and J. Davis, "Fusion of time-of-flight depth and stereo for high accuracy depth maps," In Proc. CVPR, pp. 1–8, 2008.

[11] K. Kannan, B. Rajesh Kanna and C. Aravindan, "Root mean square filter for noisy images based on hypergraph model," Image and Vision Computing, vol. 28, 2010.

[12] Mesa Imaging, SwissRanger SR3000 Manual, Version 1.02,2006, http://aiweb.techfak.unibielefeld.de/

[13] R. Garnett, T. Huegerich, C. Chui, H. Wenjie, "A universal noise removal algorithm with an impulse detector," IEEE Trans. Image Process, vol. 14(11), pp. 1747–1754, 2005.

[14] R. Dharmarajan and K. Kannan, "A hypergraph-based algorithm for image restoration from salt and pepper noise," Int. J. Electronics and Communication, 2010.

[15] Q. Ying-Dong, C. Cheng-Song, C. San-Ben, L. Jin-Quan, "A fast subpixel edge detection method using Sobel–Zernike moments operator," Image and Vision Computing, vol. 23, pp. 11–17, 2005.

[16] A. S. Awad and H. Man, "Similar neighbor criterion for impulse noise removal in images," Int. J. Electronics and Communication, vol. 64(10), pp. 904-915, 2010.

[17] H. Takeda, S. Farsiu, and P. Milanfar, "Kernel regression for image processing and reconstruction," IEEE Transactions on Image Processing, vol. 16 (2), pp. 349–366, 2007.

[18] H. Liu, C. Yang, N. Pan, E. Song, R. Green, "Denoising 3D MR images by the enhanced non-local means filter for Rician noise", Elsevier Magnetic Resonance Imaging, 2010.